CHEMISTRY OF MATERIALS

pubs.acs.org/cm

Article

Synthesis-Dependent Fluorescence Properties of $CsPbBr_2Cl$ Supercrystals

Robert Thalwitzer, Wolfgang Leis, Ross E. Carter, Elena Chulanova, Dmitry Lapkin, Gerard N. Hinsley, Bihan Wang, Kuan Hoon Ngoi, Rustam Rysov, Fabian Westermeier, Ivan A. Vartanyants, Ivan A. Zaluzhnyy, Frank Schreiber, and Marcus Scheele*

Cite This: *Chem. Mater.* 2026, 38, 2923−2932

Read Online

ACCESS | Metrics & More | Article Recommendations | Supporting Information

ABSTRACT: We compare the fluorescence properties of $CsPbBr_2Cl$ nanocrystals, obtained via two distinct synthetic procedures and self-assembled into supercrystals using the same antisolvent crystallization technique. By spatially resolved fluorescence (lifetime) measurements we demonstrate that the optical properties of the supercrystals depend on the specific synthesis conditions of the constituting nanocrystals. Using scanning electron microscopy, small-angle X-ray scattering, and nuclear magnetic resonance spectroscopy, we find evidence that spatial fluctuations in the supercrystal fluorescence correlate with the ligand sphere of the nanocrystals. Specifically, homogeneous surface passivation of the nanocrystals leads to consistent interparticle distances and increased structural order within the supercrystals, resulting in a uniform fluorescence center wavelength and lifetime. The results of this study emphasize the importance of the relationship between crystalline structure and ligand configuration in controlling the optical properties of lead halide perovskite supercrystals.

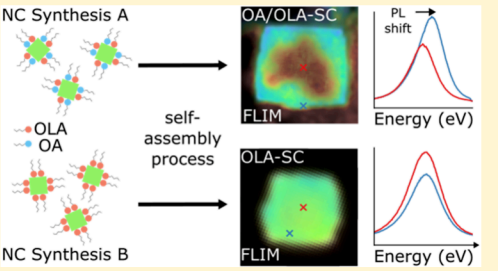

INTRODUCTION

Lead halide perovskite (LHP) nanocrystals (NCs) possess exceptional optoelectronic properties, as they exhibit an exceedingly high quantum yield[1] and the ability of a precisely tailored emission wavelength through halide composition variation.[2] This renders them promising materials for a wide range of applications in photonics and optoelectronics, including light-emitting diodes (LEDs), solar cells, and other electro-optical devices.[3−5] However, for practical applications in such devices, homogeneous fluorescence properties are of central importance to ensure uniform and reproducible electro-optical properties. In this context, so-called supercrystals (SCs)—defined as highly ordered mesoscopic aggregates of NCs—provide substantial advantages over isolated NCs and bulk phase crystals. Through collective phenomena such as superfluorescence,[6] enhanced conductivity,[4] or improved mechanical properties,[7,8] SCs transfer the unique quantum properties of NCs from the nanoscopic to the macroscopic range—an essential step for industrial applications.

A plethora of methodologies have been developed for the fabrication of SCs, encompassing solvent−antisolvent and solvent−evaporation methods.[8−19] For lead halide perovskite materials, the latter has been the prevailing technique. Nonetheless, a shift in photoluminescence is frequently observed in these SCs, although its origin is not yet fully understood.[20,21] Potential explanations for this phenomenon include compressive strain caused by drying solvents,[22] and the colloidal softness or density of organic ligands utilized for surface passivation. The influence of ligands, as well as cooperative effects between oleic acid (OA) and oleylamine (OLA) that are often used, have already been shown for $CsPbX_3$ nanocrystals.[23−27] However, their role in the formation of SCs has not yet been sufficiently investigated as the NCs exhibit a rather unusual cubic shape.[28−30] Conversely, in studies on metallic NCs, such as Au[31−33] and Ag,[34,35] or semiconducting PbS[36] and CdSe[37] nanomaterials, the ligands have been demonstrated to play a pivotal role in the self-assembly process of the SCs. Their binding motif, length, and density significantly influence the structure and properties of the resulting SC. We consider this aspect particularly relevant because of the physical and chemical interactions (i) between the ligands and the nanocrystals and (ii) between the soft ligands themselves. These interaction types influence two essential parameters that determine the properties of SCs: the lattice structure and the interparticle distances within the SCs.[38]

An alternative approach toward the formation of LHP supercrystals is inducing the crystallization via an antisolvent, such as acetonitrile.[8] However, we found that this approach

Received: December 15, 2025
Revised: February 21, 2026
Accepted: March 2, 2026
Published: March 12, 2026

https://doi.org/10.1021/acs.chemmater.5c03393
Chem. Mater. 2026, 38, 2923−2932

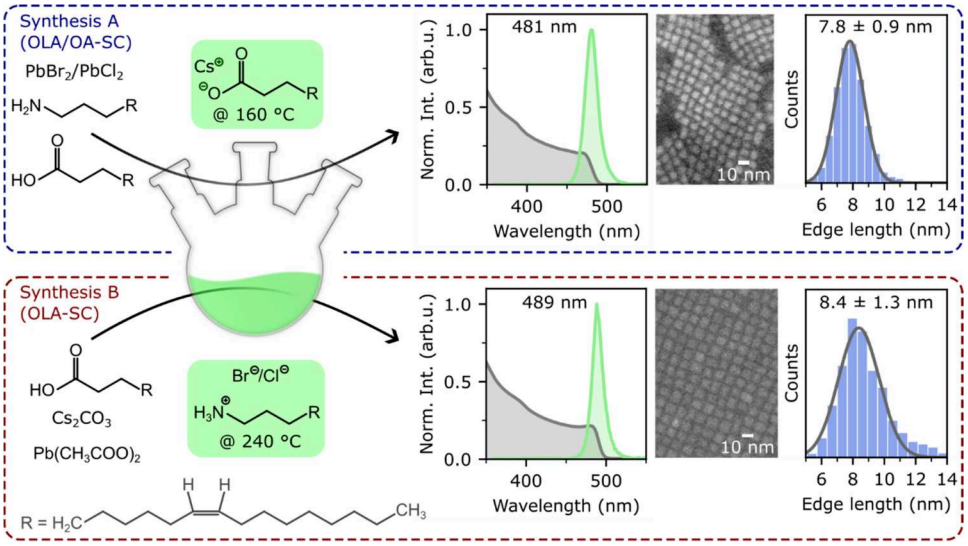

Figure 1. Overview of the two different syntheses used for NC preparation along with the absorbance and PL spectra of the respective NCs, SEM images of the NCs, and the resulting size distribution histograms. Top panel shows Synthesis A: NCs prepared according to the synthesis by Protesescu et al.[2] Bottom panel shows Synthesis B: NCs prepared according to the synthesis by Dutta et al.[40]

also frequently results in spatial fluctuations in the optical properties of the supercrystals. Diverging results by other groups—some reporting uniform fluorescence,[27] others support our observations[21,29]—have motivated us to understand the origin of this inconsistency. We hypothesize that the discrepancy may be linked to the slightly different procedures applied for the synthesis of the constituting nanocrystals rather than the crystallization method itself.

In this work, we use two sets of optically comparable $CsPbBr_2Cl$ nanocrystals, obtained by two widely employed synthetic procedures that are overall similar but differ in the intricate details of the precursor chemistry and ligand mixture. We apply scanning electron microscopy (SEM), small-angle X-ray scattering (SAXS), confocal laser scanning microscopy, and nuclear magnetic resonance (NMR) spectroscopy to probe the morphology, optical homogeneity, and molecular composition of the surface of the SCs. We show that the ligand sphere is key to obtain supercrystals with spatially uniform fluorescence and fluorescence lifetimes and that this can be controlled by the synthesis conditions of the nanocrystals.

EXPERIMENTAL SECTION

Scanning Electron Microscopy and Energy-Dispersive X-ray Spectroscopy

SEM images and energy-dispersive X-ray (EDX) data were acquired on a HITACHI SU8030 instrument at 30 kV. SEM samples of the NC stock solutions were prepared on a Si/SiO_x wafer by spin-coating 100 μL of the crude stock solution onto the wafer. SEM images of the SCs were taken directly from the crystals grown on the wafer substrates. In order to determine the thickness of the SCs, the samples were tilted 54° and 70° relative to the incident electron beam.

EDX data were analyzed using ESPRIT 1.9 software by Bruker. The background was automatically corrected by the software package. Quantification was performed using a P/B-ZAF analysis, in which the atomic concentrations of the selected elements were calculated. The analytical error of the measurements is below 3% (3-sigma confidence interval).

Nuclear Magnetic Resonance Spectroscopy

All NMR spectra were recorded at a temperature of 298 K with a Bruker Avance III HDX 600 MHz spectrometer equipped with a 5 mm Prodigy BBO cryo probe with automatic tuning and matching for X and ^{1}H, and the probe was controlled by Topspin. All ^{1}H NMR (600.13 MHz) chemical shifts are relative to 1% tetramethylsilane in deuterated chloroform via the deuterium lock.

Spatially Resolved Optical Measurements

Spatially resolved optical measurements were conducted on a home-built inverted confocal laser scanning microscope under 405 nm pulsed diode laser excitation (Picoquant LDH P-C-405) with variable repetition rates (Picoquant PDL 800-D laser driver). The measurements were performed on SCs grown on Si/SiO_x substrates with reflective geometry. The excitation laser was focused on the sample by a high numeric aperture air objective (NA = 0.9) enabling a lateral resolution of approximately 300 nm. A single-photon avalanche diode (MPD PDM Series) in combination with a PicoQuant HydraHarp 400 was used as a time-correlated single-photon counting (TCSPC) system for the time-resolved fluorescence detection. Subsequent data acquisition and analysis were performed using the SymPhoTime 64 software package by PicoQuant. Spectral data were recorded on a Andor Shamrock SR-303i-B spectrograph with a 300 grooves/mm grating equipped with an iDus 401 CCD detector (cooled to −60 °C).

Optical Measurements

Absorbance spectra were recorded on a UV−Vis−NIR spectrometer (Cary 5000, Agilent Technologies), and emission spectra were acquired using a fluorescence spectrometer (PerkinElmer PL8500). All spectra were recorded under ambient conditions at room temperature (25 °C) using 5 μL of the stock solution dispersed in 3 mL of hexane. The concentration of the NC stock solutions was calculated from the absorbance spectra using the values at 335 and 400 nm, following the method described by Maes et al.[39] The excitation wavelength for emission spectra was set to λ_{ex} = 350 nm.

X-ray Diffraction Experiments

The spatially resolved X-ray diffraction data were collected at the Coherence Applications beamline P10 of the PETRA III synchrotron source at DESY. The supercrystals were grown on a Kapton substrate, and the diffraction patterns were measured in transmission geometry by an EIGER X 4M detector placed at a distance of 5 m behind the sample. The X-ray beam of E = 12.5 keV was focused to approximately 1.5 μm × 2.1 μm (vert. x hor.).

https://doi.org/10.1021/acs.chemmater.5c03393
Chem. Mater. 2026, 38, 2923−2932

RESULTS

Figure 1 shows the two synthetic pathways employed to yield the two distinctive NC batches along with their respective optical properties and size distributions. In the case of Synthesis A, the NCs were synthesized according to the method published by Protesescu et al.,[2] wherein lead bromide and lead chloride were dissolved in the appropriate stochiometric ratio within a mixture of octadecene (ODE), oleic acid (OA), and oleylamine (OLA). The injection of cesium oleate at a temperature of 160 °C initiates the formation of the NCs. A detailed description of the synthesis can be found in the Supporting Information (Section 1: Materials and Methods). The absorption and photoluminescence (PL) spectra of the NCs show a first excitonic transition at 468 nm and a PL maximum at 481 nm with a full width at half-maximum (FWHM) of 19 nm. NC sizes were determined from SEM images by measuring the edge lengths and fitting the resulting size distributions with a Gaussian function. We find a mean size of the NCs of Synthesis A of 7.8 nm, with a standard deviation of 0.9 nm.

The NCs of Synthesis B were synthesized following the method published by Dutta et al.,[40] using oleylammonium bromide/chloride as the halide precursor that is injected into a solution of cesium carbonate and lead acetate in octadecene and oleic acid at 240 °C. These NCs show slightly higher excitonic and PL peaks at 480 and 489 nm, respectively, with the PL peak being narrower, exhibiting a FWHM of 16 nm. Based on SEM measurements, an average edge length of 8.4 ± 1.3 nm can be found by fitting the size distribution histogram with a Gaussian function. The approximately 9 nm red shift in the emission wavelength of the NCs from Synthesis B correlates with the marginal increase in the NC size as well as a slightly more bromide-rich composition of the NCs, as evident from the energy-dispersive X-ray spectroscopy (EDX) data presented in Table 1. We conclude that the optical properties and size of the NCs of the two samples are sufficiently similar to allow a fair comparison of their behavior as building blocks of SCs.

Table 1. Calculated Relative Stoichiometry of NCs from Syntheses A and B Based on Atomic Concentrations Deduced from EDX Measurements Referenced to Pb (the Analytical Error Is below 3% within a 3-Sigma Confidence Interval)

	Cs	Pb	Br	Cl
synthesis A	1.1	1.0	2.2	1.0
synthesis B	1.0	1.0	2.4	0.7

The preparation of SCs from both samples was accomplished by a self-assembly process from solution employing our modified solvent−antisolvent crystallization method.[8] In this method, a substrate is placed in a test tube, and then 600 μL of a 1−5 μM solution of the NCs in hexane and an equal volume of acetonitrile as an antisolvent are added, so the phase boundary between the two solutions is formed roughly at the middle of the substrate. The sealed test tube is left for 5 days in the dark, allowing the crystallization process to occur. The resulting SCs predominantly grow at the phase boundary between the two solvents in a cubic and highly faceted shape with lateral dimensions of approximately 15 × 15 μm^2 and a height of up to 7 μm (see Figure S5 in the Supporting Information). From here on, we refer to SCs consisting of NCs from Synthesis A as "OA/OLA-SC," and those from Synthesis B as "OLA-SC." This emphasizes their respective surface passivation with oleic acid/oleylamine (OA/OLA) and oleylamine (OLA), which we will detail further by NMR spectroscopy.

Figure 2 displays spatially resolved photoluminescence (PL) spectra of representative SCs consisting of NCs from the two different synthesis routes under 405 nm excitation in a confocal laser scanning microscope, recorded at the positions marked by white crosses in the optical microscope images in Figure 2a,d. We observe a significant red shift of 25 meV from the edges toward the center of the OA/OLA-SC. In contrast, the PL spectra acquired on an OLA-SC exhibit a consistent emission wavelength centered at 490 nm, with no detectable shift throughout the crystal. We note a further distinction in the PL intensity: While the intensity in the OA/OLA-SC declines toward the center, it increases for the OLA-SCs. This is further illustrated in the non-normalized PL spectra recorded at the edges and centers of the SCs in Figure 2c,f.

The fluorescence lifetime images of the two SCs depicted in Figure 3 were acquired under 405 nm excitation with a spatial resolution of 300 nm, and the experimental data were fitted with pixel-by-pixel biexponential decay curves. Figure 3b,d provides a representation of the corresponding PL decay curves, alongside the biexponential fit for specific positions at the center and at the edge of the SCs. In the center of the OA/OLA-SC, we find fluorescence lifetimes of around 4.0 ns which decrease to 2.8 ns approaching the edges of the SC. For the OLA-SCs, the fluorescence lifetime image indicates a uniform lifetime of about 1.8 ns over the entire crystal. This is confirmed by the PL decay curves, which result in virtually the same biexponential fits for selected points in the center and the edge of this SC.

We employed one- and two-dimensional NMR spectroscopy, in particular ^{1}H and nuclear Overhauser effect spectroscopy (NOESY), to examine the surfaces of the NCs utilized for crystallizations, as the ligands can have a significant influence on the SC formation.[23,38] NOESY spectra contain information regarding the interaction between the ligand molecules and the NC surface based on the occurrence of cross peaks in combination with their phase relative to the diagonal signals. The red color implies a positive peak intensity, and the black color implies a negative one. Given the negative diagonal peaks (black), cross peaks with the same phase, also negative, may be explained by either chemical exchange processes or NOE effects in big "molecules" (slow tumbling). With the selected mixing times of 0.1 s, NOE cross peaks should be significantly more intensive than cross peaks due to exchange. Therefore, the occurrence of rather intensive cross peaks indicates NOE between different groups of the same or of different species in the NCs surface.[41−43]

Figure 4a shows the structures of OA and OLA, which were used as ligands in the synthesis of the NCs to stabilize the surface. We focus here on the chemical environment of the different head groups to serve as indicators for the binding interactions of the ligands with the NCs. For the OLA, we label the protons of the NH_3^+ group and the neighboring CH_2 group with "α" and "β", respectively. For OA, we use the labels "1" and "2" for the two methylene-groups closest to the carbonyl group. In Figure 4b, the ^{1}H NMR spectrum of the NCs of Synthesis A is depicted alongside the spectrum of oleic acid as a reference. Compared with the reference spectrum, signal 1 at

https://doi.org/10.1021/acs.chemmater.5c03393
Chem. Mater. 2026, 38, 2923−2932

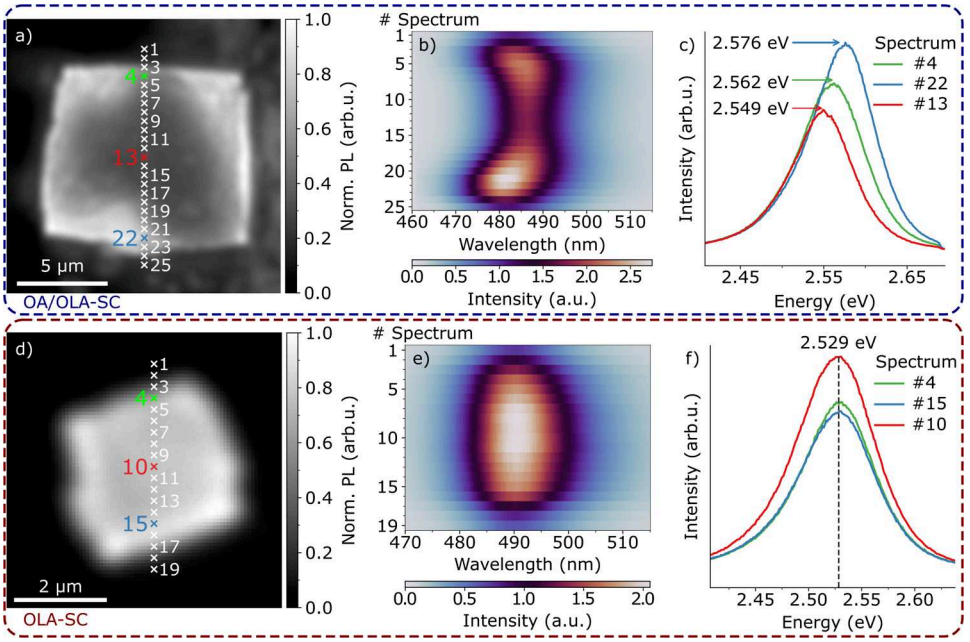

Figure 2. Spatially resolved fluorescence of $CsPbBr_2Cl$ OA/OLA-SC (a–c) and OLA-SC (d–f). (a, d) PL intensity images of a $CsPbBr_2Cl$ OA/OLA-SC and an OLA-SC. (b, e) PL spectra measured at the indicated positions in the PL intensity image in panel (a,d). (c, f) PL spectra recorded at selected positions at the center and the edges of the SCs.

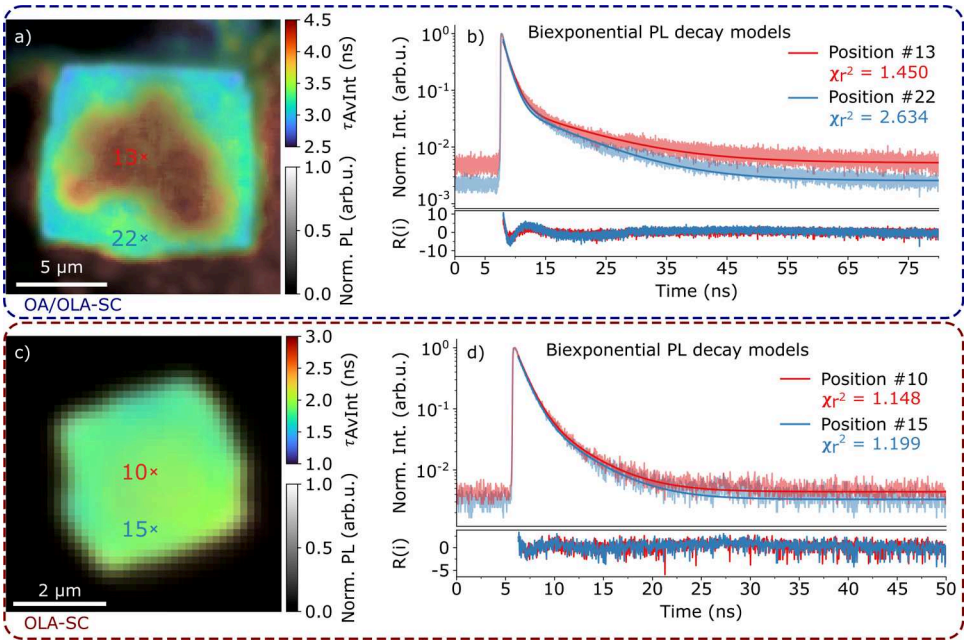

Figure 3. Spatially resolved fluorescence lifetime imaging of $CsPbBr_2Cl$ OA/OLA-SC (a, b) and OLA-SC (c, d). (a, c) Fluorescence lifetime images of the SCs. Experimental time-resolved fluorescence data are fitted with a biexponential decay function. (b, d) Normalized fluorescence lifetime histogram at selected positions at the center (red) and the edge (blue) of the supercrystal fitted with a biexponential decay function. The weighted residuals $R(i)$ indicate the deviation between experimental data and the biexponential fit, and χr^2 represents the goodness of the biexponential fit model.

2.35 ppm demonstrates a significant broadening accompanied by the loss of the fine structure of the triplet. The broadened signals at 6.9 and 3.5 ppm, respectively, are assigned to α and β. Furthermore, at 4.9 and 5.9 ppm, distinct multiplets can be discerned, which can be attributed to the CH_2 groups and the terminal double bond of 1-octadecene, which is typically used as a high-boiling-point solvent in NC synthesis. From the NOESY spectrum of the NCs of Synthesis A in Figure 4c, the appearance of rather intensive cross peaks between signals of characteristic groups of OLA or OA and signals of CH_2 groups of the residue (R) suggests that both ligands are in the surface layer of the NCs, which is consistent with literature.[42] Hence, the SCs prepared from these NCs were termed "OA/OLA-SCs."

The ^{1}H NMR spectrum of the NCs from Synthesis B (see Figure 5a) reveals broadened α and β signals at 6.8 and 3.5 ppm, respectively. Contrary to the results of Synthesis A, signal 1 emerges as a well-resolved triplet at 2.4 ppm, which does not

https://doi.org/10.1021/acs.chemmater.5c03393
Chem. Mater. 2026, 38, 2923−2932

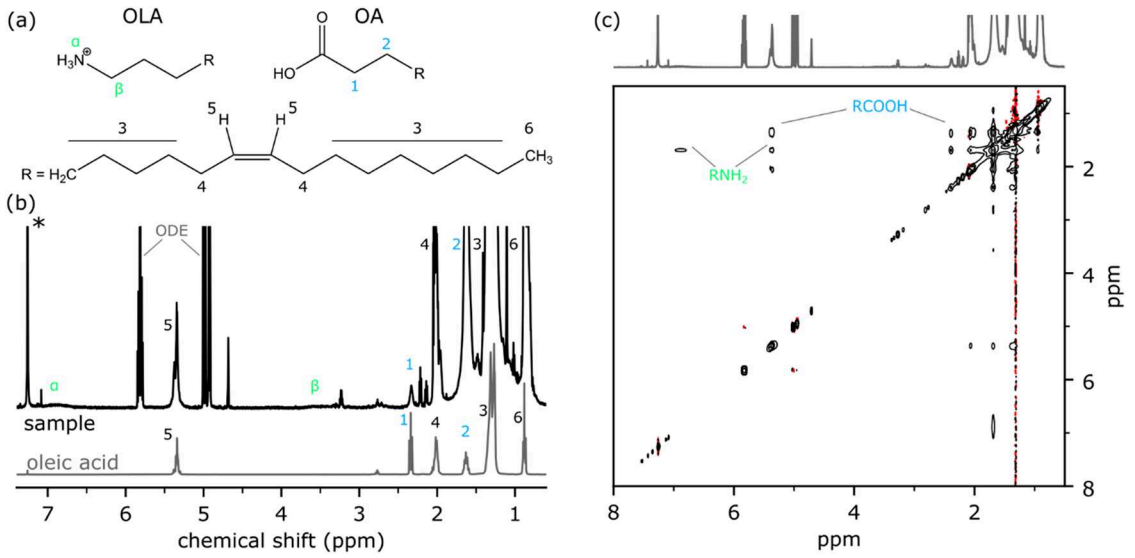

Figure 4. NMR spectra of $CsPbBr_2Cl$ NCs from Synthesis A. (a) Chemical formula of oleic acid (OA) and oleylamine (OLA) used as ligands in the synthesis of the NCs. (b) ^1H NMR spectrum of the $CsPbBr_2Cl$ NC solution in $CDCl_3$ and oleic acid as reference. Signals are assigned to protons of the ligands as indicated in (a). (c) 2D-NOESY NMR spectrum of the $CsPbBr_2Cl$ NC solution in $CDCl_3$.

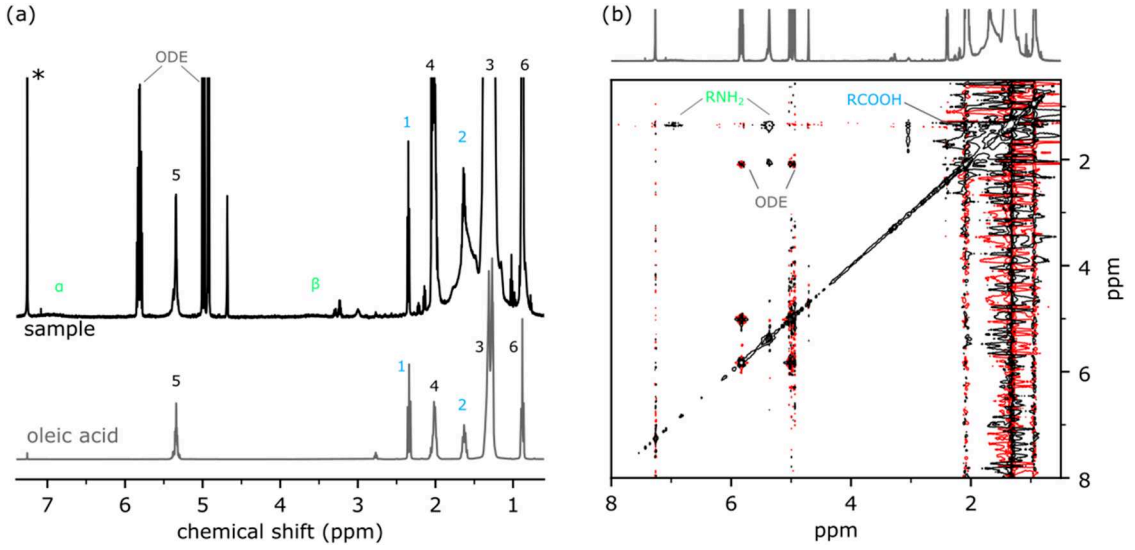

Figure 5. NMR Spectroscopy of $CsPbBr_2Cl$ NCs from Synthesis B. (a) ^1H NMR spectrum of the $CsPbBr_2Cl$ NC solution in $CDCl_3$ and oleic acid as reference. Signals are assigned to protons of the ligands as indicated in Figure 4a. (b) 2D-NOESY NMR spectrum of the $CsPbBr_2Cl$ NC solution in $CDCl_3$.

display any discernible cross peaks in the NOESY spectrum (Figure 5b). The coloration of the observed weak signal shows an antiphase (positive and negative) pattern, indicating a significant contribution of *J* coupling between the groups, but not the binding of OA to the NC surface.[41,43] The same applies to the cross peaks of ODE. In contrast, the rather intense negative cross peaks between the characteristic OLA signals and the CH_2 groups of the residue (R) imply an interaction of this ligand with the NC surface. Therefore, the SCs prepared from these NCs were termed "OLA-SCs."

To correlate the optical properties with the structure of the SCs, we performed SEM (Figure 6) and SAXS (Figure 7) of SCs grown from both NC solutions. We note that the same OLA-SC was used for the SEM analysis in Figure 6d as for the optical measurements in Figures 2d and 3c. The SCs display high structural order and an increase of NC size from the edge toward the center regardless of which synthesis is used to obtain the comprising NCs. While the mean size of the NCs at the edges of the SCs matches the size in the stock solution (6.9 ± 0.7 nm for OA/OLA-SCs and 8.3 ± 0.7 nm for OLA-SCs), it increases within the first few hundred nanometers to its maximum value (13.8 ± 1.1 nm for OA/OLA-SCs and 15.2 ± 1.0 nm for OLA-SCs) as evident from Figure S5 in the SI. Within each region, the size distribution remains relatively narrow. We attribute this to a stepwise increase in the NC size, as inferred from examining a monolayer of NCs remaining on the growth substrate after mechanical lifting of an SC from the substrate (see Figure S6 in the SI for further details). Although this is, at first, an unexpected finding when considering the often cited size purification effect during self-assembly[44,45] and the relatively narrow size distributions of both NC stock

https://doi.org/10.1021/acs.chemmater.5c03393
Chem. Mater. 2026, 38, 2923−2932

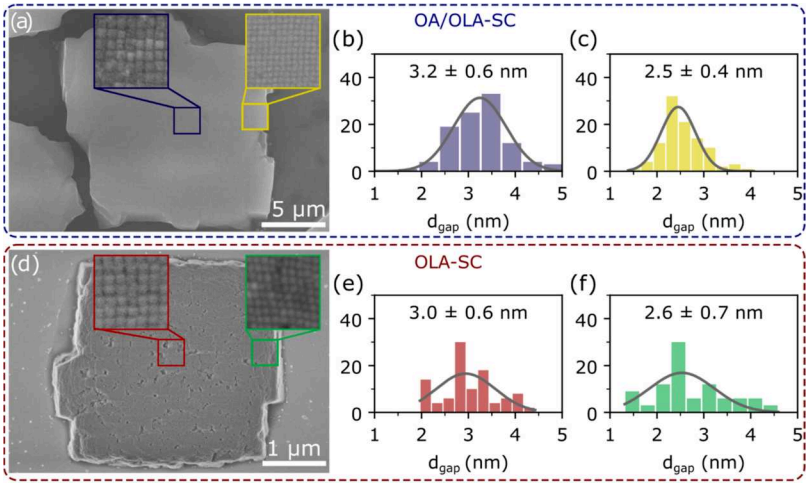

Figure 6. Interparticle distances d_{gap} derived from SEM images by measuring the edge-to-edge distances. All values are obtained by fitting the histogram data with a Gaussian function (gray curve). (a, d) SEM images of an OA/OLA-SC and an OLA-SC, respectively. Insets display the magnified images of the regions of interest. (b, e) Interparticle distances in the center of the SC. (c, f) Interparticle distances at the edges of the SC.

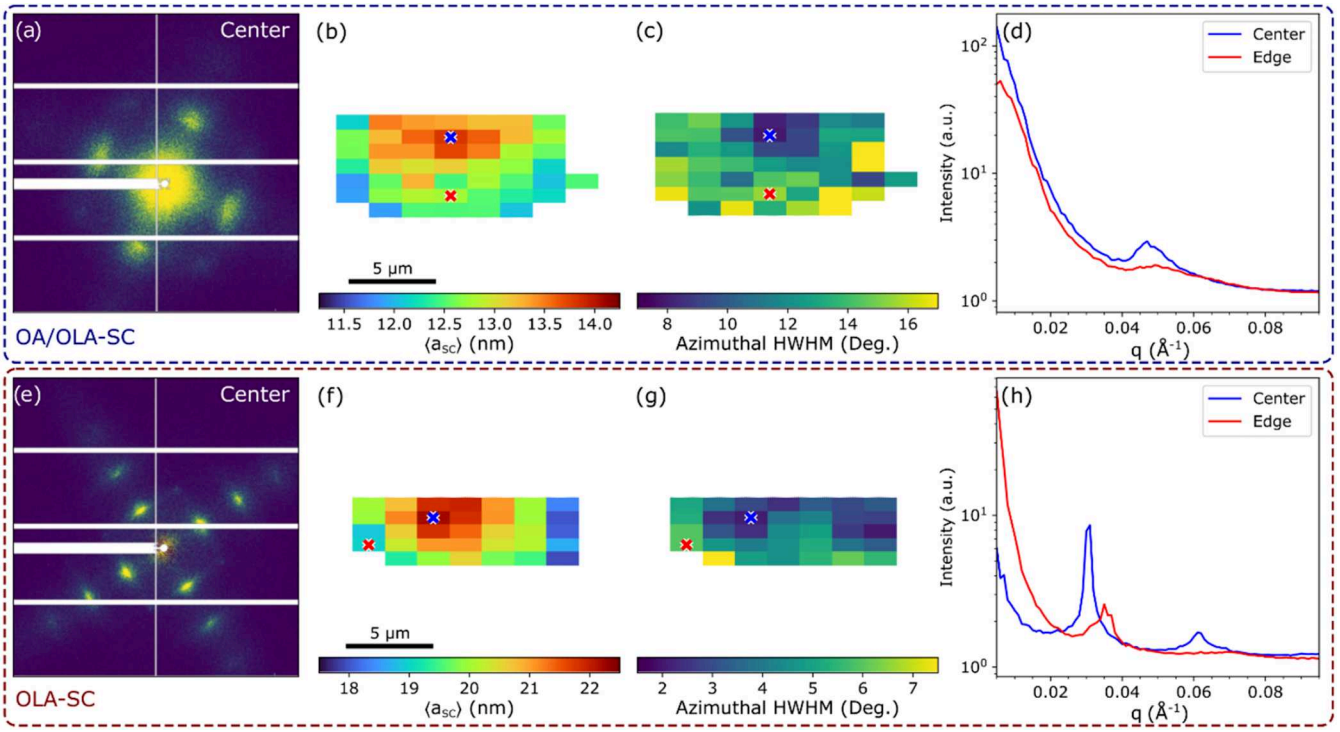

Figure 7. Spatially resolved X-ray scattering of an OA/OLA-SC (a–d) and an OLA-SC (e–h). (a, e) Diffraction patterns taken from the center of the SCs. (b, f) Spatial map of the SC unit cell parameter. (c, g) Spatial map of the azimuthal HWHM, averaged over four first-order SAXS peaks. (d, h) Radial intensity at the center and edge of the SC marked by blue and red crosses, respectively.

solutions, these results are consistent with a previous report on similar SCs.[8]

In Figure 6b,c,e,f, we evaluated the interparticle distances (d_{gap}) within the SCs both centrally and peripherally by using the SEM images shown in Figure 6a,d. To this end, we measured the edge-to-edge distances of adjacent NCs and fitted the resulting histograms with a Gaussian function (gray curve). Toward the edges of the OA/OLA-SC, the distance between the NCs decreases by 0.7 nm from 3.2 ± 0.6 to 2.5 ± 0.4 nm. In contrast, the interparticle distances in the center of the OLA-SC are slightly shorter with 3.0 ± 0.6 nm and decrease only marginally by 0.4 to 2.6 ± 0.7 nm when approaching the edges.

We corroborated our structural analysis with spatially resolved SAXS on Kapton substrates with a step size of 1 μm × 2 μm (vert. x hor.). By scanning the whole crystal, transforming each SAXS pattern into reciprocal polar coordinates (q, ϕ), and subsequently fitting the first-order SAXS peaks with 2D Gaussians, we extracted the radial and azimuthal peak positions (q_0, ϕ_0) along with their widths (Δq, $\Delta\phi$) and intensity. Figure 7a,e shows diffraction patterns of an OA/OLA-SC and an OLA-SC taken at the center of the SCs. Using the equation $\langle a_{SC}\rangle = 2\pi/q_0$, where q_0 is the position of

https://doi.org/10.1021/acs.chemmater.5c03393
Chem. Mater. 2026, 38, 2923−2932

the first-order SAXS peaks, we obtained spatially resolved maps of the average center-to-center distances of the SCs (Figure 7b,f). We note that $\langle a_{SC} \rangle$ contains not only the size of the individual NCs but also the dimensions of the ligand shell. Both maps, for the OLA-SC and the OA/OLA-SC, exhibit a gradient of $\langle a_{SC} \rangle$ from the edges to the center. The unit cell parameter $\langle a_{SC} \rangle$ along the edges of the OLA-SC is notably larger compared to those in the SEM images. This discrepancy can be attributed to the focus size of the X-ray beam employed in the SAXS measurements, which results in an average diffraction pattern of the edge region that contains NCs with different sizes. In addition, the larger NCs in this range exhibit stronger scattering such that their contribution to $\langle a_{SC} \rangle$ will dominate, suggesting an overestimation of particle sizes at the edges.

Furthermore, we calculated the azimuthal half width at half-maximum (HWHM) of $\Delta\phi$ for the first-order SAXS peaks as a measure for orientational order in the SCs. The resulting spatially resolved maps in Figure 7c,g reveal a decreasing orientational order from the center toward the edge for both SCs. Notably, the HWHM values for the OA/OLA-SC are twice as large as those for the OLA-SC.

In general, the SAXS peaks from the OLA-SCs are significantly narrower than the corresponding peaks of the OA/OLA-SCs. We exemplify this with the radial width of the peaks Δq (Figure 7d,h) for selected positions in the center and at the edges of the corresponding SCs (marked by red and blue crosses in Figure 7b,f).

DISCUSSION

Our NMR measurements (Figures 4 and 5) demonstrate that the surface chemistry of the $CsPbBr_2Cl$ nanocrystals is strongly influenced by the synthetic route, giving rise to distinct ligand environments that ultimately determine the optical homogeneity of the resulting SCs. In Synthesis A, OA and OLA likely coexist as an acid−base pair, leading to a heterogeneous mixture of both oleylammonium and oleate species bound to the NC surface. In contrast, Synthesis B employs oleylammonium bromide/chloride as a precursor, which preferentially binds to the surface, while OA remains largely unbound in solution. This difference results in a more uniform, oleylamine-only ligand shell for Synthesis B.

Regarding the expected optical properties of the SCs, we note that especially the PL lifetime depends on several factors. In general, it is positively correlated with the NC size due to a growing contribution of a symmetry forbidden (s-p) transition in larger NCs (>8 nm) at room temperature.[46−48] This would explain the lifetime gradient in the OA/OLA-SCs (Figure 3a). Interparticle coupling and strain-induced optical inhomogeneities further affect the optical characteristics. In the case of the OLA-SCs, we hold the homogeneous surface passivation responsible for the spatially constant photoluminescence (PL) wavelength (Figure 2e,f) and lifetime (Figure 3c), potentially by enabling consistent interparticle coupling and suppressing strain.

The structural analyses by SEM corroborate this interpretation. SCs composed of uniformly OLA-passivated NCs display comparatively weakly varying interparticle distances from the edges to the center (Figure 6d−f). In contrast, OA/OLA-SCs exhibit a more pronounced gradient—larger separations in the center that decrease toward the edges (Figure 6a−c). This deviation is approximately twice as large in the mixed-ligand system, suggesting that uneven surface coverage leads to differential compressibility and, potentially, local strain. We suggest that this contributes to the observed blue shift and shorter fluorescence lifetimes in the edge regions of the OA/OLA-SCs.

These observations can be rationalized within the framework of the Orbifold Topological Model (OTM),[49,50] which describes NCs as hard cores surrounded by a deformable ligand shell. Two parameters are particularly relevant: the grafting density, which quantifies how densely ligands pack on the surface, and the colloidal softness parameter $\lambda = 2d/l_E$, defined by the ratio of the ligand length d to the edge length of the NC core l_E. Since OA and OLA possess comparable chain lengths (~2.3 nm),[50] the grafting density becomes the decisive parameter. OA exhibits a weaker binding strength to lead halide perovskites compared to OLA,[42] resulting in a lower grafting density and hence a more disordered, mobile ligand shell.[32] According to the OTM, this increased mobility enhances the effective colloidal softness and facilitates local rearrangements under strain, yielding less rigid and less uniformly packed superlattices.

We attribute the apparent decrease in grafting density to the presence of acetonitrile that we used as part of our antisolvent crystallization method. Due to its weaker binding affinity, OA is expected to desorb preferentially during crystallization, reducing the overall ligand coverage in OA/OLA-SCs to a greater extent than in OLA-SCs. This reduced surface protection may trigger localized Ostwald ripening, where smaller NCs dissolve and redeposit on larger ones, thereby generating the observed size gradient across the supercrystals.

Such a process is consistent with both the SEM and SAXS results: OA/OLA-SCs show broadened and blurred diffraction peaks as well as a larger azimuthal HWHM—signatures of increased orientational disorder[51]—whereas the OLA-SCs exhibit sharper peaks and a smaller azimuthal HWHM indicative of a well-ordered lattice.

CONCLUSIONS

Our results demonstrate that the surface chemistry of $CsPbBr_2Cl$ nanocrystals and consequently the optical and structural homogeneity of their supercrystals are critically determined by the synthesis pathway and the resulting ligand environment. The comparison between Synthesis A and Synthesis B reveals that a mixed OA/OLA surface leads to heterogeneous ligand binding, lower grafting density, and increased colloidal softness, and we propose that this structural disorder promotes strain-induced optical inhomogeneities. Conversely, the uniform oleylamine passivation achieved in Synthesis B results in densely packed superlattices with well-defined morphology and spatially consistent photoluminescence.

Supercrystals with such homogeneous optical characteristics are a prerequisite for application in electro-optical devices such as LEDs, electro-optical modulators, or narrow-line width lasers.

ASSOCIATED CONTENT

Supporting Information

The Supporting Information is available free of charge at https://pubs.acs.org/doi/10.1021/acs.chemmater.5c03393.

Synthesis and optical properties of nanocrystals in solution, detailed analysis of SEM data of supercrystals,

https://doi.org/10.1021/acs.chemmater.5c03393
Chem. Mater. 2026, 38, 2923−2932

and additional optical measurements of an OLA-SC (PDF)

AUTHOR INFORMATION

Corresponding Author

Marcus Scheele − *Institute of Physical and Theoretical Chemistry, University of Tübingen, 72076 Tübingen, Germany;* orcid.org/0000-0002-2704-3591; Email: marcus.scheele@uni-tuebingen.de

Authors

Robert Thalwitzer − *Institute of Physical and Theoretical Chemistry, University of Tübingen, 72076 Tübingen, Germany*

Wolfgang Leis − *Institute of Physical and Theoretical Chemistry, University of Tübingen, 72076 Tübingen, Germany*

Ross E. Carter − *Institute of Applied Physics, University of Tübingen, 72076 Tübingen, Germany;* orcid.org/0009-0007-5891-2853

Elena Chulanova − *Institute of Applied Physics, University of Tübingen, 72076 Tübingen, Germany;* Present Address: Chemistry Research Laboratory, 12 Mansfield Road, Oxford OX1 3TA, U.K; orcid.org/0000-0001-5452-6831

Dmitry Lapkin − *Institute of Applied Physics, University of Tübingen, 72076 Tübingen, Germany*

Gerard N. Hinsley − *Deutsches Elektronen-Synchrotron DESY, 22607 Hamburg, Germany;* orcid.org/0000-0002-3793-6094

Bihan Wang − *Deutsches Elektronen-Synchrotron DESY, 22607 Hamburg, Germany*

Kuan Hoon Ngoi − *Deutsches Elektronen-Synchrotron DESY, 22607 Hamburg, Germany;* orcid.org/0009-0003-0502-0721

Rustam Rysov − *European X-Ray Free Electron Laser Facility GmbH, 22869 Schenefeld, Germany*

Fabian Westermeier − *Deutsches Elektronen-Synchrotron DESY, 22607 Hamburg, Germany;* orcid.org/0000-0003-0696-206X

Ivan A. Vartanyants − *Deutsches Elektronen-Synchrotron DESY, 22607 Hamburg, Germany;* orcid.org/0000-0002-0340-8234

Ivan A. Zaluzhnyy − *Institute of Applied Physics, University of Tübingen, 72076 Tübingen, Germany;* orcid.org/0000-0001-5946-2777

Frank Schreiber − *Institute of Applied Physics, University of Tübingen, 72076 Tübingen, Germany;* orcid.org/0000-0003-3659-6718

Complete contact information is available at: https://pubs.acs.org/10.1021/acs.chemmater.5c03393

Notes

The authors declare no competing financial interest.

ACKNOWLEDGMENTS

We thank Jonathan de Roo for fruitful discussions. Funding for this work was provided by the Deutsche Forschungsgemeinschaft (DFG) under grants SCHE1905/15-1 (project no. 546072194) and SCHR700/47-1 (project no. 546072194) and the Volkswagen Foundation under project no. 0072510-00. The authors acknowledge DESY (Hamburg, Germany) for the provision of experimental facilities. Parts of this research were carried out at PETRA III synchrotron facility, and we would like to thank the beamline staff, especially Michael Sprung, for the assistance in using the Coherence Applications P10 beamline. Beamtime was allocated for proposal I-20220813.

REFERENCES

(1) Imran, M.; Caligiuri, V.; Wang, M.; Goldoni, L.; Prato, M.; Krahne, R.; De Trizio, L.; Manna, L. Benzoyl Halides as Alternative Precursors for the Colloidal Synthesis of Lead-Based Halide Perovskite Nanocrystals. *J. Am. Chem. Soc.* **2018**, *140*, 2656−2664.

(2) Protesescu, L.; Yakunin, S.; Bodnarchuk, M. I.; Krieg, F.; Caputo, R.; Hendon, C. H.; Yang, R. X.; Walsh, A.; Kovalenko, M. V. Nanocrystals of Cesium Lead Halide Perovskites (CsPbX3, X = Cl, Br, and I): Novel Optoelectronic Materials Showing Bright Emission with Wide Color Gamut. *Nano Lett.* **2015**, *15*, 3692−3696.

(3) Polavarapu, L.; Nickel, B.; Feldmann, J.; Urban, A. S. Advances in Quantum-Confined Perovskite Nanocrystals for Optoelectronics. *Adv. Energy Mater.* **2017**, *7*, No. 1700267.

(4) Kirsch, C.; Naujoks, T.; Haizmann, P.; Frech, P.; Peisert, H.; Chassé, T.; Brütting, W.; Scheele, M. Zwitterionic Carbazole Ligands Enhance the Stability and Performance of Perovskite Nanocrystals in Light-Emitting Diodes. *ACS Appl. Mater. Interfaces* **2023**, *15*, 32744−32752.

(5) Akkerman, Q. A.; Rainò, G.; Kovalenko, M. V.; Manna, L. Genesis, challenges and opportunities for colloidal lead halide perovskite nanocrystals. *Nat. Mater.* **2018**, *17*, 394−405.

(6) Rainò, G.; Becker, M. A.; Bodnarchuk, M. I.; Mahrt, R. F.; Kovalenko, M. V.; Stöferle, T. Superfluorescence from lead halide perovskite quantum dot superlattices. *Nature* **2018**, *563*, 671−675.

(7) Dreyer, A.; Feld, A.; Kornowski, A.; Yilmaz, E. D.; Noei, H.; Meyer, A.; Krekeler, T.; Jiao, C.; Stierle, A.; Abetz, V.; et al. Organically linked iron oxide nanoparticle supercrystals with exceptional isotropic mechanical properties. *Nat. Mater.* **2016**, *15*, 522−528.

(8) Hiller, J. L.; Thalwitzer, R.; Bozkurt, A.; Ferreira, M. G.; Hodak, R.; Strauß, F.; Nadler, E.; Hinsley, G. N.; Wang, B.; Ngoi, K. H.; et al. Mechanically Robust Supercrystals from Antisolvent-Induced Assembly of Perovskite Nanocrystals. *ACS Nano* **2025**, *19*, 26117−26126.

(9) Murray, C. B.; Kagan, C. R.; Bawendi, M. G. Self-Organization of CdSe Nanocrystallites into Three-Dimensional Quantum Dot Superlattices. *Science* **1995**, *270*, 1335−1338.

(10) Murray, C. B.; Kagan, C. R.; Bawendi, M. G. Synthesis and Characterization of Monodisperse Nanocrystals and Close-Packed Nanocrystal Assemblies. *Annu. Rev. Mater. Res.* **2000**, *30*, 545−610.

(11) Talapin, D. V.; Shevchenko, E. V.; Kornowski, A.; Gaponik, N.; Haase, M.; Rogach, A. L.; Weller, H. A New Approach to Crystallization of CdSe Nanoparticles into Ordered Three-Dimensional Superlattices. *Adv. Mater.* **2001**, *13*, 1868−1871.

(12) Rogach, A. L.; Talapin, D. V.; Shevchenko, E. V.; Kornowski, A.; Haase, M.; Weller, H. Organization of Matter on Different Size Scales: Monodisperse Nanocrystals and Their Superstructures. *Adv. Funct. Mater.* **2002**, *12*, 653−664.

(13) Rupich, S. M.; Shevchenko, E. V.; Bodnarchuk, M. I.; Lee, B.; Talapin, D. V. Size-Dependent Multiple Twinning in Nanocrystal Superlattices. *J. Am. Chem. Soc.* **2010**, *132*, 289−296.

(14) Vanmaekelbergh, D. Self-assembly of colloidal nanocrystals as route to novel classes of nanostructured materials. *Nano Today* **2011**, *6*, 419−437.

(15) Baranov, D.; Toso, S.; Imran, M.; Manna, L. Investigation into the Photoluminescence Red Shift in Cesium Lead Bromide Nanocrystal Superlattices. *J. Phys. Chem. Lett.* **2019**, *10*, 655−660.

(16) Baranov, D.; Fieramosca, A.; Yang, R. X.; Polimeno, L.; Lerario, G.; Toso, S.; Giansante, C.; Giorgi, M. D.; Tan, L. Z.; Sanvitto, D.; Manna, L. Aging of Self-Assembled Lead Halide Perovskite Nanocrystal Superlattices: Effects on Photoluminescence and Energy Transfer. *ACS Nano* **2021**, *15*, 650−664.

(17) Cherniukh, I.; Rainò, G.; Stöferle, T.; Burian, M.; Travesset, A.; Naumenko, D.; Amenitsch, H.; Erni, R.; Mahrt, R. F.; Bodnarchuk, M. I.; Kovalenko, M. V. Perovskite-type superlattices from lead halide perovskite nanocubes. *Nature* **2021**, *593*, 535−542.
(18) Fang, Y.; Wei, H.; Dong, Q.; Huang, J. Quantification of re-absorption and re-emission processes to determine photon recycling efficiency in perovskite single crystals. *Nat. Commun.* **2017**, *8*, No. 14417.
(19) Ferreira, M. G.; Gastin, B.; Hiller, J.; Zaluzhnyy, I. A.; Hinsley, G. N.; Wang, B.; Ngoi, K. H.; Vartanyants, I. A.; Schreiber, F.; Scheele, M.; Baranov, D. Self-Assembly of Quantum-Confined CsPbBr3 Perovskite Nanocrystals into Rhombic, Frame, and Rectangular Superlattices. *Small Struct.* **2025**, *6*, No. 2500133.
(20) Lapkin, D.; Kirsch, C.; Hiller, J.; Andrienko, D.; Assalauova, D.; Braun, K.; Carnis, J.; Kim, Y. Y.; Mandal, M.; Maier, A.; et al. Spatially resolved fluorescence of caesium lead halide perovskite supercrystals reveals quasi-atomic behavior of nanocrystals. *Nat. Commun.* **2022**, *13*, No. 892.
(21) Levy, S.; Be'er, O.; Veber, N.; Monachon, C.; Bekenstein, Y. Tuning the Colloidal Softness of CsPbBr3 Nanocrystals for Homogeneous Superlattices. *Nano Lett.* **2023**, *23*, 7129−7134.
(22) Kapuscinski, M.; Agthe, M.; Lv, Z.-P.; Liu, Y.; Segad, M.; Bergström, L. Temporal Evolution of Superlattice Contraction and Defect-Induced Strain Anisotropy in Mesocrystals during Nanocube Self-Assembly. *ACS Nano* **2020**, *14*, 5337−5347.
(23) Udayabhaskararao, T.; Houben, L.; Cohen, H.; Menahem, M.; Pinkas, I.; Avram, L.; Wolf, T.; Teitelboim, A.; Leskes, M.; Yaffe, O.; et al. A Mechanistic Study of Phase Transformation in Perovskite Nanocrystals Driven by Ligand Passivation. *Chem. Mater.* **2018**, *30*, 84−93.
(24) Sun, S.; Yuan, D.; Xu, Y.; Wang, A.; Deng, Z. Ligand-Mediated Synthesis of Shape-Controlled Cesium Lead Halide Perovskite Nanocrystals via Reprecipitation Process at Room Temperature. *ACS Nano* **2016**, *10*, 3648−3657.
(25) Shamsi, J.; Dang, Z.; Bianchini, P.; Canale, C.; Di Stasio, F.; Brescia, R.; Prato, M.; Manna, L. Colloidal Synthesis of Quantum Confined Single Crystal CsPbBr3 Nanosheets with Lateral Size Control up to the Micrometer Range. *J. Am. Chem. Soc.* **2016**, *138*, 7240−7243.
(26) Pan, A.; He, B.; Fan, X.; Liu, Z.; Urban, J. J.; Alivisatos, A. P.; He, L.; Liu, Y. Insight into the Ligand-Mediated Synthesis of Colloidal CsPbBr3 Perovskite Nanocrystals: The Role of Organic Acid, Base, and Cesium Precursors. *ACS Nano* **2016**, *10*, 7943−7954.
(27) Imran, M.; Ijaz, P.; Baranov, D.; Goldoni, L.; Petralanda, U.; Akkerman, Q.; Abdelhady, A. L.; Prato, M.; Bianchini, P.; Infante, I.; Manna, L. Shape-Pure, Nearly Monodispersed CsPbBr3 Nanocubes Prepared Using Secondary Aliphatic Amines. *Nano Lett.* **2018**, *18*, 7822−7831.
(28) Hallstrom, J.; Cherniukh, I.; Zha, X.; Kovalenko, M. V.; Travesset, A. Ligand Effects in Assembly of Cubic and Spherical Nanocrystals: Applications to Packing of Perovskite Nanocubes. *ACS Nano* **2023**, *17*, 7219−7228.
(29) Boehme, S. C.; Bodnarchuk, M. I.; Burian, M.; Bertolotti, F.; Cherniukh, I.; Bernasconi, C.; Zhu, C.; Erni, R.; Amenitsch, H.; Naumenko, D.; et al. Strongly Confined CsPbBr3 Quantum Dots as Quantum Emitters and Building Blocks for Rhombic Superlattices. *ACS Nano* **2023**, *17*, 2089−2100.
(30) Filippi, U.; Toso, S.; Zaffalon, M. L.; Pianetti, A.; Li, Z.; Marras, S.; Goldoni, L.; Meinardi, F.; Brovelli, S.; Baranov, D.; Manna, L. Cooling-Induced Order−Disorder Phase Transition in CsPbBr3 Nanocrystal Superlattices. *Adv. Mater.* **2025**, *37*, No. 2410949.
(31) Prasad, B. L. V.; Stoeva, S. I.; Sorensen, C. M.; Klabunde, K. J. Digestive-Ripening Agents for Gold Nanoparticles: Alternatives to Thiols. *Chem. Mater.* **2003**, *15*, 935−942.
(32) Badia, A.; Singh, S.; Demers, L.; Cuccia, L.; Brown, G. R.; Lennox, R. B. Self-Assembled Monolayers on Gold Nanoparticles. *Chem. - Eur. J.* **1996**, *2*, 359−363.
(33) Boles, M. A.; Talapin, D. V. Many-Body Effects in Nanocrystal Superlattices: Departure from Sphere Packing Explains Stability of Binary Phases. *J. Am. Chem. Soc.* **2015**, *137*, 4494−4502.
(34) Lee, Y. H.; Shi, W.; Lee, H. K.; Jiang, R.; Phang, I. Y.; Cui, Y.; Isa, L.; Yang, Y.; Wang, J.; Li, S.; Ling, X. Y. Nanoscale surface chemistry directs the tunable assembly of silver octahedra into three two-dimensional plasmonic superlattices. *Nat. Commun.* **2015**, *6*, No. 6990.
(35) Zhang, X.; Lv, L.; Ji, L.; Guo, G.; Liu, L.; Han, D.; Wang, B.; Tu, Y.; Hu, J.; Yang, D.; Dong, A. Self-Assembly of One-Dimensional Nanocrystal Superlattice Chains Mediated by Molecular Clusters. *J. Am. Chem. Soc.* **2016**, *138*, 3290−3293.
(36) Lokteva, I.; Dartsch, M.; Dallari, F.; Westermeier, F.; Walther, M.; Grübel, G.; Lehmkühler, F. Real-Time X-ray Scattering Discovers Rich Phase Behavior in PbS Nanocrystal Superlattices during In Situ Assembly. *Chem. Mater.* **2021**, *33*, 6553−6563.
(37) Baranov, D.; Fiore, A.; van Huis, M.; Giannini, C.; Falqui, A.; Lafont, U.; Zandbergen, H.; Zanella, M.; Cingolani, R.; Manna, L. Assembly of Colloidal Semiconductor Nanorods in Solution by Depletion Attraction. *Nano Lett.* **2010**, *10*, 743−749.
(38) Si, K. J.; Chen, Y.; Shi, Q.; Cheng, W. Nanoparticle Superlattices: The Roles of Soft Ligands. *Adv. Sci.* **2018**, *5*, No. 1700179.
(39) Maes, J.; Balcaen, L.; Drijvers, E.; Zhao, Q.; De Roo, J.; Vantomme, A.; Vanhaecke, F.; Geiregat, P.; Hens, Z. Light Absorption Coefficient of CsPbBr3 Perovskite Nanocrystals. *J. Phys. Chem. Lett.* **2018**, *9*, 3093−3097.
(40) Dutta, A.; Behera, R. K.; Pal, P.; Baitalik, S.; Pradhan, N. Near-Unity Photoluminescence Quantum Efficiency for All CsPbX3 (X = Cl, Br, and I) Perovskite Nanocrystals: A Generic Synthesis Approach. *Angew. Chem.* **2019**, *131*, 5608−5612.
(41) Hens, Z.; Martins, J. C. A Solution NMR Toolbox for Characterizing the Surface Chemistry of Colloidal Nanocrystals. *Chem. Mater.* **2013**, *25*, 1211−1221.
(42) De Roo, J.; Ibáñez, M.; Geiregat, P.; Nedelcu, G.; Walravens, W.; Maes, J.; Martins, J. C.; Van Driessche, I.; Kovalenko, M. V.; Hens, Z. Highly Dynamic Ligand Binding and Light Absorption Coefficient of Cesium Lead Bromide Perovskite Nanocrystals. *ACS Nano* **2016**, *10*, 2071−2081.
(43) Grisorio, R.; Di Clemente, M. E.; Fanizza, E.; Allegretta, I.; Altamura, D.; Striccoli, M.; Terzano, R.; Giannini, C.; Irimia-Vladu, M.; Suranna, G. P. Exploring the surface chemistry of cesium lead halide perovskite nanocrystals. *Nanoscale* **2019**, *11*, 986−999.
(44) Bertolotti, F.; Vivani, A.; Ferri, F.; Anzini, P.; Cervellino, A.; Bodnarchuk, M. I.; Nedelcu, G.; Bernasconi, C.; Kovalenko, M. V.; Masciocchi, N.; Guagliardi, A. Size Segregation and Atomic Structural Coherence in Spontaneous Assemblies of Colloidal Cesium Lead Halide Nanocrystals. *Chem. Mater.* **2022**, *34*, 594−608.
(45) Clark, D. E.; Lumsargis, V. A.; Blach, D. D.; Zhu, K.; Shumski, A. J.; Yao, L.; Chen, Q.; Huang, L.; Li, C. W. Quantifying Structural Heterogeneity in Individual CsPbBr3 Quantum Dot Superlattices. *Chem. Mater.* **2022**, *34*, 10200−10207.
(46) Krieg, F.; Sercel, P. C.; Burian, M.; Andrusiv, H.; Bodnarchuk, M. I.; Stöferle, T.; Mahrt, R. F.; Naumenko, D.; Amenitsch, H.; Rainò, G.; Kovalenko, M. V. Monodisperse Long-Chain Sulfobetaine-Capped CsPbBr3 Nanocrystals and Their Superfluorescent Assemblies. *ACS Cent. Sci.* **2021**, *7*, 135−144.
(47) Abbas, A. S.; Chabeda, D.; Weinberg, D.; Limmer, D. T.; Rabani, E.; Alivisatos, A. P. Non-monotonic size-dependent exciton radiative lifetime in CsPbBr3 nanocrystals. *Nat. Commun.* **2025**, *16*, No. 6401.
(48) Zhu, C.; Boehme, S. C.; Feld, L. G.; Moskalenko, A.; Dirin, D. N.; Mahrt, R. F.; Stöferle, T.; Bodnarchuk, M. I.; Efros, A. L.; Sercel, P. C.; et al. Single-photon superradiance in individual caesium lead halide quantum dots. *Nature* **2024**, *626*, 535−541.
(49) Travesset, A. Topological structure prediction in binary nanoparticle superlattices. *Soft Matter* **2017**, *13*, 147−157.

https://doi.org/10.1021/acs.chemmater.5c03393
Chem. Mater. 2026, 38, 2923−2932

(50) Travesset, A. Soft Skyrmions, Spontaneous Valence and Selection Rules in Nanoparticle Superlattices. *ACS Nano* **2017**, *11*, 5375−5382.
(51) Ondry, J. C.; Frechette, L. B.; Geissler, P. L.; Alivisatos, A. P. Trade-offs between Translational and Orientational Order in 2D Superlattices of Polygonal Nanocrystals with Differing Edge Count. *Nano Lett.* **2022**, *22*, 389−395.

https://doi.org/10.1021/acs.chemmater.5c03393
Chem. Mater. 2026, 38, 2923−2932